



A Fan Spine Jet: Nonradial Filament Eruption and the Plasmoid Formation

Haidong Li^{1,2} and Jiayan Yang^{1,2}

¹ Yunnan Observatories, Chinese Academy of Sciences, 396 Yangfangwang, Guandu District, Kunming, 650216, People's Republic of China; lhd@ynao.ac.cn

² Center for Astronomical Mega-Science, Chinese Academy of Sciences, 20A Datun Road, Chaoyang District, Beijing, 100012, People's Republic of China

Received 2018 June 15; revised 2018 December 21; accepted 2018 December 21; published 2019 February 13

Abstract

Using the data from *SDO* and *NVST*, we studied a circular filament eruption in association with the formation of jet under a nonaxisymmetric fan spine configuration. A nonradial motion of the filament toward a null point and the formation of a jet were presented in detail. This event contained a small circular filament, which was located above the polarity inversion line. The nonlinear force-free field extrapolation shows the presence of a nonaxisymmetric fan spine structure above the filament. Thus, the filament was confined by this magnetic field structure. Since the confining magnetic pressure decreases much faster toward the null point than anywhere else, the filament displayed a shift motion toward the null point that resulted in a collision, and a reconnection signature of bidirectional flows was observed. Due to the external magnetic reconnection, the topology of the filament field was reconfigured, accompanying by the scattered filament material spreading along nearby coronal loops, which resulted in a blowout jet. Particularly, some ejected plasma blobs were also observed in the vicinity of the interfaces between the filament and neighboring coronal loops. These blobs originating from the dissipation region may be plasmoids in association with tearing mode instability. We suggested that in pre-jet phase the nonaxisymmetric fan spine configuration can act on the erupting filament, laterally deflecting and channeling its motion toward the null point, which may facilitate the jet formation by magnetic reconnection.

Key words: Sun: activity – Sun: corona – Sun: filaments, prominences

Supporting material: animations

1. Introduction

Solar jets are transient, collimated plasma ejections along open fields or the legs of large-scale coronal loops. They are observed in X-rays and at a variety of extreme-ultraviolet (EUV) wavelengths (Shimojo et al. 1996; Cirtain et al. 2007; Nisticò et al. 2009), reflecting the fact that some jets possess both hot and cool components. Shen et al. (2012) showed that the cool component of the jet is formed by a small eruptive filament at the jet base, while the hot component resulted from the heated plasma during the reconnection between the filament and the ambient magnetic field. In 3D simulations, jet models invoke reconnection between regions of locally closed and locally open field as the jet-generation mechanism (Wyper et al. 2016). The reconnection process is always associated with some brightening blobs near the junction between the jet spire and the arch base, which is considered as the signature of the tearing mode instability (Furth et al. 1963; Kliem et al. 2000; Asai et al. 2004; Lin et al. 2005; Ni et al. 2012; Kumar & Cho 2013; Wyper et al. 2016; Zhang et al. 2016; Shen et al. 2017; Zhang & Zhang 2017). It is because of magnetic reconnection that the filament structure is destroyed and the material in it is blown out along overlying loops, resulting in a jet (Li et al. 2017).

The distribution of the magnetic field for jets is usually multipolar (Moreno-Insertis et al. 2008; Kumar et al. 2018). In numerical simulations, reconnection-driven coronal jets are always considered as an embedded bipole magnetic field topology, and magnetic energy in this system can be built up and released (Pariat et al. 2009, 2010, 2015; Wyper & DeVore 2016; Wyper et al. 2016). Magnetic extrapolation of the sources of a UV and X-ray jet (Fletcher et al. 2001; Moreno-Insertis et al. 2008) has associated the classical anemone structure of the jets (Shibata et al. 1992; Shimojo et al. 1996; Jiang et al. 2007; Yang et al. 2011;

Hong et al. 2017; Shen et al. 2018a, 2018b) with a 3D fan spine topology, in which a magnetic null point is a preferred site for reconnection (Pontin et al. 2004; Pontin & Galsgaard 2007; Priest & Pontin 2009). A small-scale filament under this type of magnetic configuration eventually erupted, taking the shape of a jet (Li et al. 2017; Kumar et al. 2018). Such a scenario was summarized by Wyper et al. (2017), who pointed out that the breakout model for solar eruptions could explain small-scale jets. In fan spine topology, due to the complexity of the magnetic field, the ambient field around the null dome is not always perpendicular to the plane of the sky, resulting in a nonaxisymmetric set of closed loops below the dome. Pariat et al. (2010) suggested that a jet process is always dominated by a synthetic role from magnetic geometrical characteristics of the jet source: size, flux distribution, location of the null, and asymmetry. Many observations found that jets could appear with similar morphology and outflow (Nisticò et al. 2009; Zhang et al. 2012) but might possess distinctive dynamical properties in the low coronal source region before the jet phase. Essentially, the equilibrium of a filament embedded in an overlying magnetic field is determined by two competing effects: the outward-directed magnetic pressure between the filament and photosphere, and the inward-directed magnetic tension of the overlying field. The imbalance of forces can lead to filament eruption. In large-scale filament eruption, some strong deflections of filament are reported in a quadrupolar system (Bemporad et al. 2005; Jiang et al. 2009; Bi et al. 2013). The deflection of filament may be related to global magnetic configuration force imbalances, which are caused by a nonuniform distribution of the background magnetic field energy density (Shen et al. 2011). Since a small-scale filament eruption of a fan spine is always related to the jet formation (Hong et al. 2017; Li et al. 2017, 2018a, 2018b; Xu et al. 2017), it is necessary to study the dynamical process of a filament under a fan dome.

Our event clearly showed that the nonradial motion started at the beginning of the filament eruption, which was indeed related to a nonaxisymmetric fan spine configuration. The overlying field can exert an effect on a filament and so guide its eruption. This provides us with the possibility of detailing the relationship between such a nonradial filament eruption, a nonaxisymmetric fan spine, and the resulting jet. The paper is organized as follows. In Section 2, we describe the observations and magnetic field modeling. In Section 3 we present the eruption of the circular filament and the formation of the jet, and in Section 4 we present external magnetic reconnection between the filament and the overlying loops and the associated plasma blobs. We summarize our findings and discuss the interpretation of the fan spine jet in Section 5.

2. Observations and Magnetic Field Modeling

The filament eruption is well covered by observations from the *Solar Dynamics Observatory* (*SDO*; Pesnell et al. 2012) and the New Vacuum Solar Telescope (NVST; Liu & Beckers 2001; Liu et al. 2014). For the *SDO*, the Atmospheric Imaging Assembly (AIA; Lemen et al. 2012) multiwavelength images and the Helioseismic and Magnetic Imager (HMI; Schou et al. 2012) data are chosen to study the event. AIA has nine passbands for observational data, with a pixel resolution of 0''.6 and 12 s cadence for the EUV passbands and 24 s for the UV passbands, while HMI magnetograms have a pixel resolution of 0''.5 and 45 s cadence. The H α data with a higher pixel resolution of 0''.165 and higher cadence of 12 s are also obtained by NVST. In addition, *Fermi* satellites provide the soft X-ray and hard X-ray (HXR) fluxes of the eruptive event.

We choose the vector magnetogram for extrapolation at 08:48 UT prior to the eruption from the HMI AR Patches (SHARP; Bobra et al. 2014). The observed data are computed by the Very Fast Inversion of the Stokes Vector code (Borrero et al. 2011), and the remaining 180° azimuth ambiguity is resolved by the Minimum Energy method (Metcalfe 1994; Leka et al. 2009). In addition, a preprocessing procedure is performed to drive the data toward suitable boundary conditions (Wiegelmann et al. 2006). Using the nonlinear force-free magnetic field (NLFFF) package available in SolarSoftWare (SSW), the 3D coronal magnetic fields is extrapolated by the optimization method of Wheatland et al. (2000) and Wiegelmann (2004). The calculation is carried out within a box of $70 \times 60 \times 256$ uniformly spaced grid points with $\Delta x = \Delta y = \Delta z = 0''.5$.

3. The Eruption of a Circular Filament and the Formation of the Jet

Figure 1 presents the overview of the events. In the NVST H α image, a circular filament with an apparent length of 18 Mm and a width of about 3 Mm appeared at the edge of the sunspot of AR 12002 (indicated in Figure 1(b)). Comparing the HMI magnetogram with the H α image, it is found that the long axis of the filament is located between an isolated positive pole (P) and surrounding negative fields (N). Based on the hot channel at AIA 94 Å, we can identify that the eruptive filament occurred near one footpoint of large-scale coronal loops (indicated in Figure 1(d)). After that, the eruption caused a remote brightening taking place at another end of coronal loops as shown at AIA 304 Å in Figure 4(c).

Figure 2 shows the process of the eruption filament interacting with the coronal loops and the jet formation. From the NVST observation, we can see that the filament rose up from the lying site moving laterally from northwest to southeast toward the coronal loops (Figures 2(b)–(c)). During the lateral motion, an anticlockwise rotation of the filament was observed when viewed from above (Figure 3). The obvious rotational motion started at around 08:55 UT and ended at around 09:04 UT. The direction is represented by the white arrow in Figure 3(a). The rotation of the filament was also revealed by the transverse movement of some strands, which was obviously seen in the H α time slice in Figure 3(d). From the trajectory of movement of one strand, it can be estimated that the filament rotated about 1.1 turns. Accompanied by the rotation, some fine dark threads moved as a whole from the southeast to the northwest to the coronal loops (Figures 2(a)–(f)). At last, most of the threads interacted with the overlying field (see also Figure 4(f)). In this process, a circular ribbon developed at the site of filament eruption as indicated in Figures 2(b) and (e). By 09:04 UT, an interaction between the shifting filament and the coronal loops occurred and a brightening of the filament appeared at the reconnection sites (indicated by the white arrow in Figure 2(f)). The brightened plasma around the reconnection region may be heated to higher temperature. Meanwhile, the reconnection resulted in the formation of some newly closed hot loops connecting “P” to “N1” (indicated in Figure 2(i)). From AIA 304 Å observations at 09:06 UT, the filament was split and disintegrated completely. It is clear that the draining process is not freely falling but shaped by the magnetic field, and the bulk of filament mass flowed away along the nearby magnetic field, taking the shape of a jet (Figures 2(g) and (h)).

Two enhancements of EUV/UV emission occurred during the filament eruption. In Figure 4(a), we present the light curves taken from a small region crossing the erupting region, which experienced two energy release stages. For the light curves at AIA 304 and 1600 Å, a small peak around 08:56 UT may correspond to the first phase of energy release. The second stage started at 09:01 UT, and the light curves of AIA 94, 304, and 1600 Å show a sharp peak between 09:04 and 09:07 UT. We found that the peak time of AIA 94 Å lags behind the peak time of AIA 304 and 1600 Å by about 2–3 minutes. Thus, it could be a complicated heating phenomenon. Additionally, the cold chromospheric AIA 304 Å emission shows the impulsive enhancement, almost coincident with the *Fermi* 10–14 and 14–25 keV HXR emission peak, as well as the flare ribbon emission from AIA 1600 Å. This implies that the chromosphere may be heated by high-energy electrons involving magnetic reconnection. We also measured the evolution of the positive flux in the active region, which displays a continuous magnetic flux decrease from 08:55 to 09:10 UT. Such a changing flux pattern suggests that the cancellation between the negative polarity and the encircled positive polarity occurred during the formation of the jet.

In Figure 4(c), we present the chronological observation of the eruptive filament shift movement toward the coronal loops through slice1 in Figure 2(c). This slit “image” is composed of strips cut from H α images, which clearly show two expansion phases of the filament. In the first phase, the filament started to rise at 08:53 UT. We measured the speed of this eruption and found it to be 149 km s^{-1} . After that, the speed of the filament decelerated obviously, and then with a constant speed

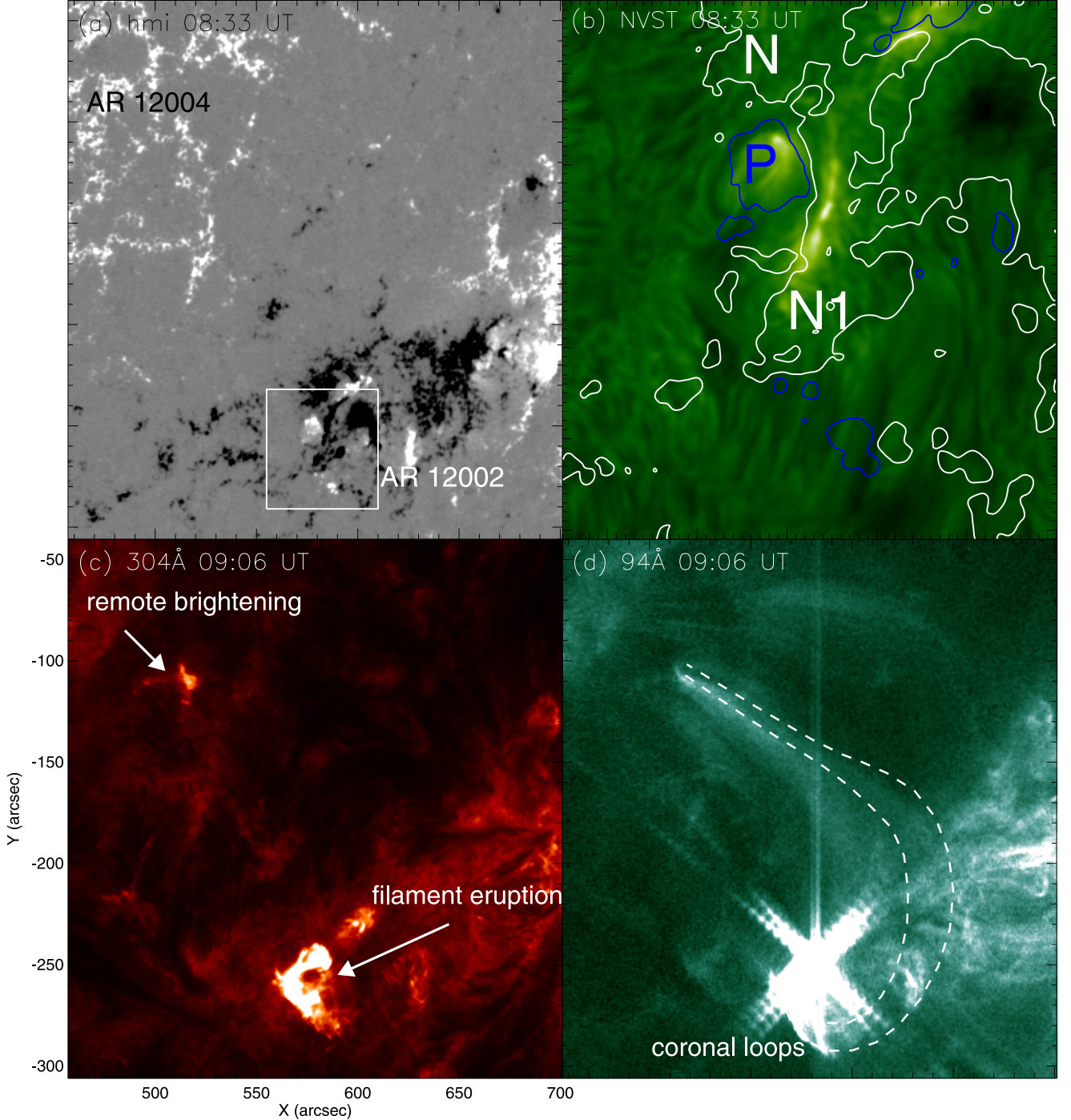


Figure 1. Overview for the studied event. (a) HMI magnetogram presenting the magnetic configuration under a circular filament. (b) NVST H α line-centered image, which belongs to the white box subregion of panel (a). The blue and white curves in panel (b) are the contours of the positive and negative polarity magnetic fields, with contour levels of ± 80 G, respectively. The letters “P” and “N” register the positive and negative polarity at each side of the filament, respectively, while “N1” indicates a footpoint of nearby coronal loops as shown in panel (d). (c) AIA 304 Å image showing a filament eruption associated with an accompanying remote brightening. (d) AIA 94 Å image showing the site of filament eruption at one footpoint of large-scale coronal loops; the dashed lines tracing the coronal loops are superposed on it. The white box indicates the field of view (FOV) for Figure 2.

of 11 km s^{-1} rising slowly. In the second phase after 09:02 UT, the filament started to speed up and then interacted with the coronal loops with a speed of 69 km s^{-1} . The later phase of the rising filament caused obvious emission enhancement (Figure 4(a)). We interpret the brightenings as the signature of external reconnection of the filament.

4. External Magnetic Reconnection and the Associated Plasma Blobs

Of particular interest for this event is the bidirectional flows and the associated plasma blobs. Figure 4(d) shows the shift motions of the filament toward the coronal loops in detail. As the filament got close to the coronal loops at 09:04 UT, some

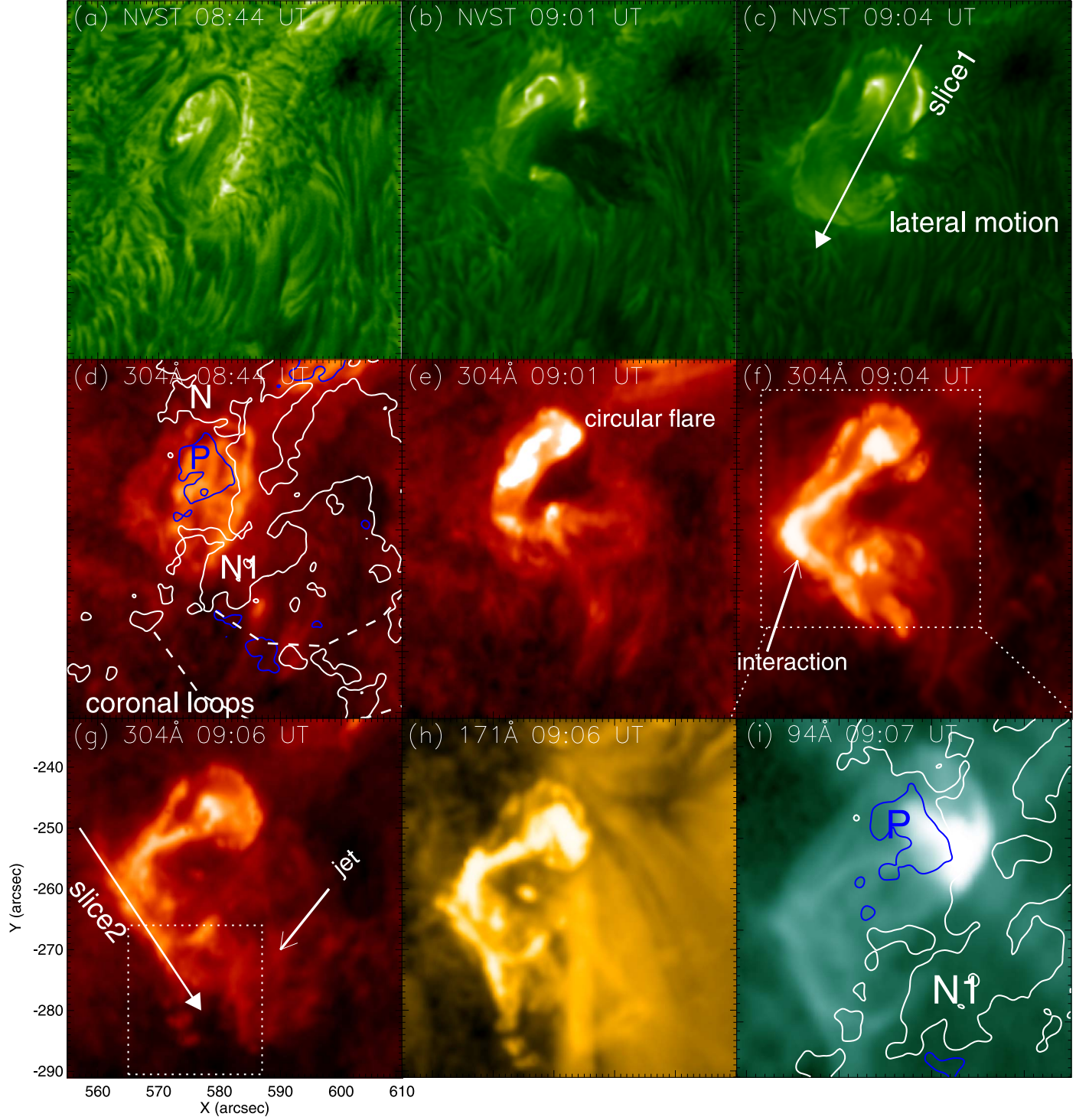


Figure 2. AIA 94, 304 Å, and H α images showing the eruptive process of the filament and subsequent interaction between the filament and coronal loops. (a–c) H α images showing the filament eruption. The solid arrow in panel (c) denotes the shift movement of the filament during filament rising. (d–g) 304 Å images showing the eruptive filament colliding with coronal loops. The blue and white contours have the same meaning as in Figure 1. The coronal loops originating from “N1” are superposed with white lines, such as in panel (d) of Figure 1. (h, i) Close-up views of the interacting region at AIA 304 and 94 Å, for which the FOV is indicated by the dashed line box in panel (f). Panel (i) is a 94 Å image showing newly formed hot loops. The white lines with an arrow (slice1 and slice2) mark the slit position of time slices as shown in Figure 3 (c) and (f), respectively. The white box of panel (g) indicates the FOV for Figure 4. The animated version of this figure compares the AIA 94, 211, and 304 Å images from 08:40 to 09:10 UT compressed to a 5 s movie.

(An animation of this figure is available.)

brightening signatures appeared as indicated by the arrow in Figure 4(e). Meanwhile, bidirectional flows occurred (see Figure 4(f)). Figure 4(f) is composed of strips cut from 94 Å

images through slice2 in Figure 2(g), displaying outward motions of bright (hot) plasma. The plasma flow velocities lie in the range of 50–324 km s $^{-1}$, which are consistent with other

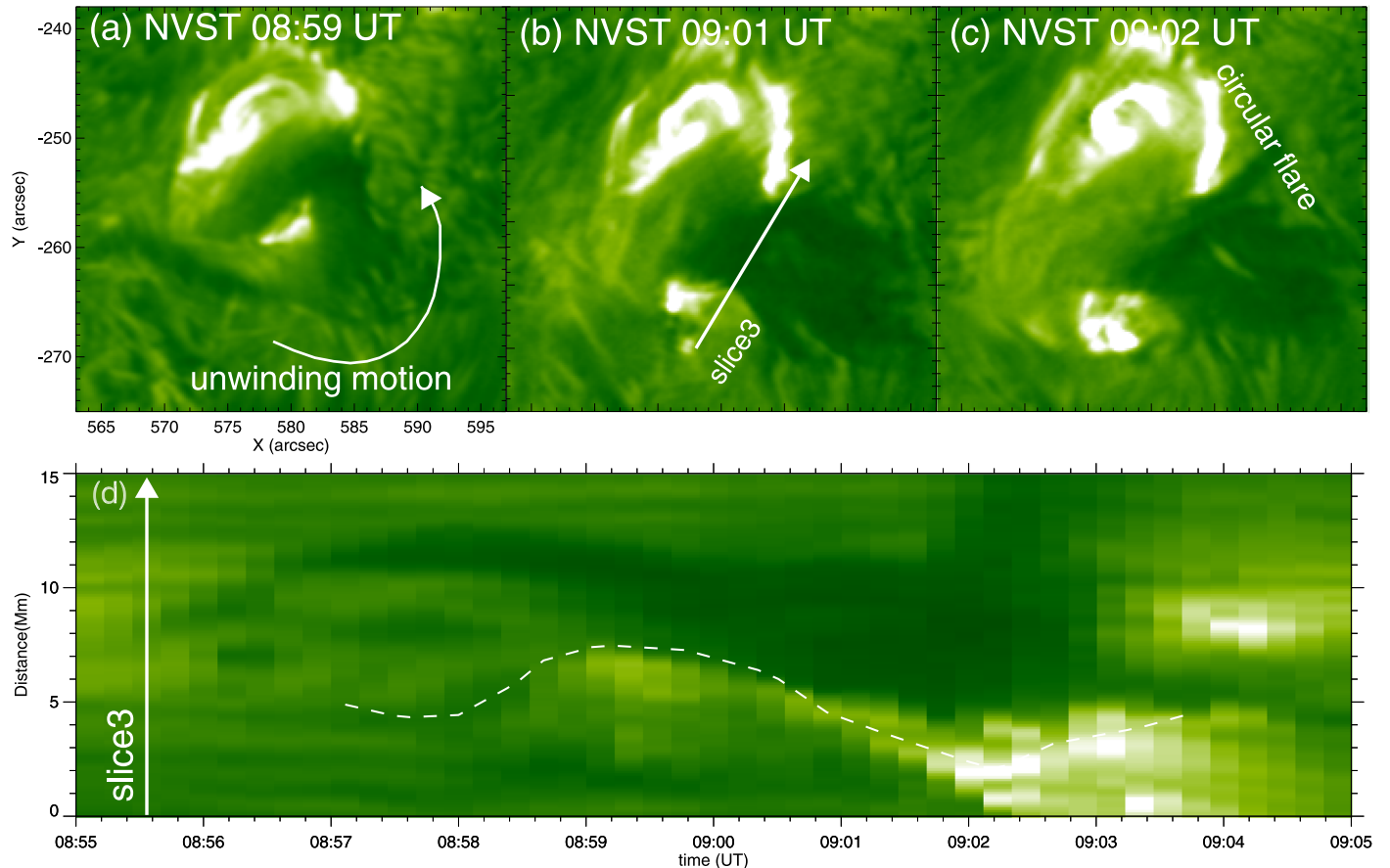


Figure 3. (a–c) H α images showing an unwinding motion of filament (counterclockwise from above). A curved arrow indicates the direction. (d) Time slice taken from H α images at the position marked by slice3 in panel (b). A strand rotating around the filament is highlighted by the white dotted line.

observations (Asai et al. 2004; Takasao et al. 2012). We also observed many plasma blobs near the reconnection region. From 09:06:23 UT to 09:07:11 UT, about 2 minutes after the filament–loop interaction, we found that multiple plasma blobs were ejected from the interaction sites successively. The typical size of the bright and compact features is about 2 Mm, moving with a fast speed (Figure 5). They have a lifetime of 60 s before merging with the background plasma and disappearing. The detailed ejection process was displayed in the animation associated with Figure 5.

Using six AIA EUV channels at 94, 335, 211, 193, 171, and 131 Å, we performed the emission measure and the temperature maps of the multiple plasmoids at 09:06:47 UT (Figures 5(e)–(f)) (Cheng et al. 2012). We found that the estimated average temperature for one of these plasmoids within the selected regions (indicated by the white box) is about 6.6 MK. In Figure 5(g), the broad differential emission measure curve implies that the plasmoid is a multitemperature structure. Its peak temperature is about 6.8 MK, which is higher than the temperature of the surrounding field.

5. Discussion and Interpretation

In this paper, we studied a filament eruption in association with the formation of a jet on 2014 March 17. There was a circular filament eruption at the edge of the active region. The eruptive filament interacted with the overlying field, resulting in the disintegration of the filament, which caused the formation of

a blowout jet and a remote brightening. In the process, the filament underwent a lateral motion toward the southeast direction to the coronal loops. Some ejected plasma blobs were also observed in the vicinity of the interfaces between the filament and neighboring coronal loops.

With the aid of the HMI vector magnetograms, we carried out an NLFFF extrapolation to reconstruct the coronal magnetic field of the jet eruption region. Figure 6 shows the consequence of the NLFFF extrapolation. We find a low-lying sheared field structure above the polarity inversion line (PIL) in Figure 6(a). Its morphology agrees well with the circular filament observed in the AIA 304 Å and H α (Figure 6(b)). Using the trilinear null finding method of Haynes & Parnell (2007) to scan the NLFFF-modeled field, we find a null point associated with a fan spine configuration. The height of the null is roughly 6 Mm from the photosphere. We also note that the asymmetrical photospheric flux distribution led to an inclined fan spine geometry. From Figure 6(c), we see that the null point is not located above the reconstructed filament, but at the southeast of the filament. The ambient, confining magnetic pressure ($P_B = B^2/8\pi$) drops off much faster in the eruption direction (null point direction) than that in other directions (Figure 6(d)). Therefore, it seems that the significant deflection was related to the null point.

Solar large-scale nonradial filament eruptions are often observed at an early stage of coronal mass ejections (CMEs; Jiang et al. 2009; Shen et al. 2011), while small-scale counterparts are rarely reported, especially in a fan spine system. In the large-scale

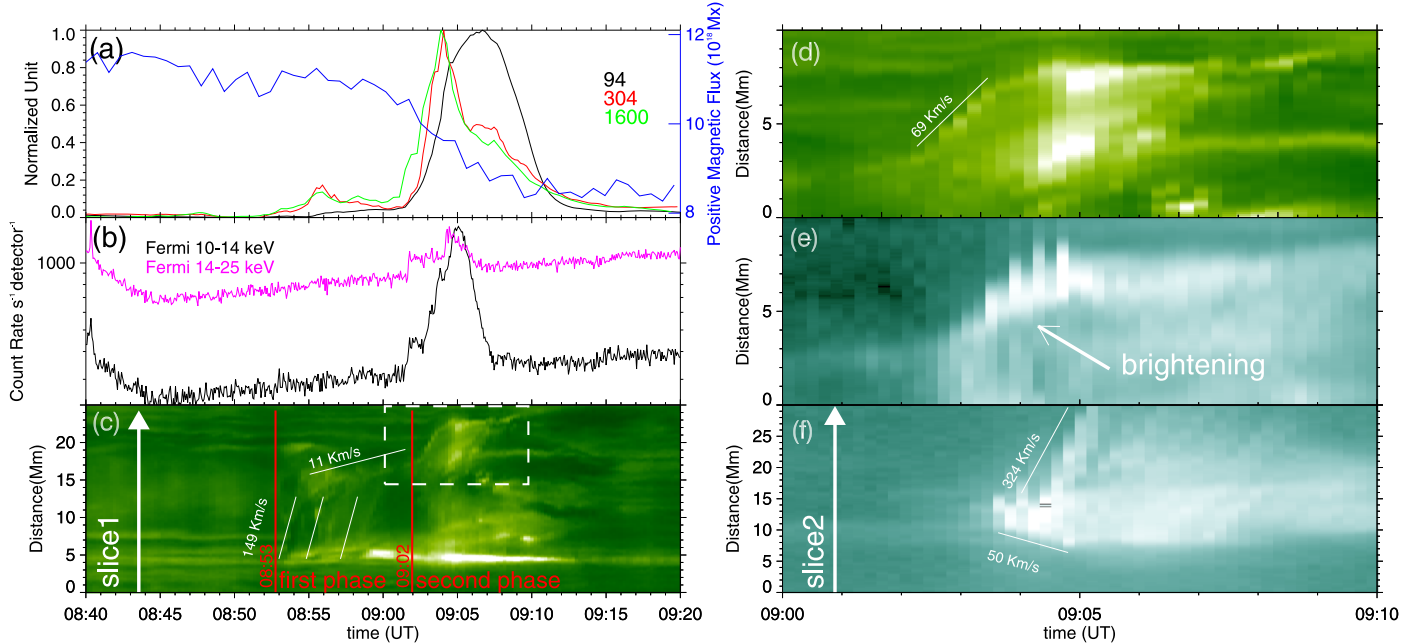


Figure 4. (a, b) Normalized light curves of AIA 94, 304, 335, and 1600 Å, and the positive magnetic flux. *Fermi* HXR 10–14 keV and 14–25 keV fluxes are also plotted. The AIA curves and magnetic flux are calculated from the eruptive region outlined by the white box in panel (f) of Figure 2(c). (c) Time-slice plot for the shift motion of the eruptive filament along slice1 in Figure 2(c), with the white lines marking the filament threads. The two vertical dashed lines (red) indicate two phases of filament expansion. (d, e) Close-up views of panel (c) at H α and 94 Å, for which the FOV is indicated by the dashed line box in panel (c). (f) Time-slice plot for the position of collision along the slice in Figure 2(g). By performing linear fitting to the stripes in these time slices, the velocities of the shift movement of the filament and the bidirectional flows from the interacting region are estimated.

case, the nonradial motion of the filament is related to global magnetic configuration force imbalances. Shen et al. (2011) suggested that filaments tend to propagate to the region with lower magnetic energy density owing to a nonuniform distribution of the background magnetic field energy density. In a streamer or pseudostreamer, the guiding action of the coronal magnetic field can deflect the filament eruption (Bemporad et al. 2005; Moore & Sterling 2007; Jiang et al. 2009). Previous studies involving a nonradial motion with a null point strongly suggest that the nonradial motion of an eruption was facilitated by the reconnection taking place near the coronal null point in a quadrupolar system (Sun et al. 2012; Bi et al. 2013). In our case, the filament eruption occurred in a nonaxisymmetric fan spine configuration, leading to the formation of a blowout jet. Before the formation of the jet, the filament underwent a nonradial motion toward the null point and then interacted with the null point and the fan spine. Such a reconnection scenario was recently emphasized in the production of solar jets (Wyper et al. 2017, 2018).

In a jet driven by the eruption of the filament, the magnetic structure may influence the trigger threshold for the jet. As reported by Pariat et al. (2010), the closed field under a fan dome is broadly twisted, to the point that the kink instability is set off, kinking the entire closed-field region. They suggested that fast reconnection onset is sensitive to the system details and that the exact criterion for fast reconnection onset relies on the inclination angles of the spine field line. The jet can be initiated after injection of a smaller twist (0.85) in a closed field under a fan dome. In our case, we cannot find any magnetic flux emergence or canceling before the filament eruption; however, a rotation of the filament larger than one turn was observed. We inferred that the kink instability may play an

important role in onset of the filament. The destabilization of the underlying small-scale filament under a nonaxisymmetric fan spine configuration is still needed to confirm with more research.

When the filament arrived at the top of the separatrix between the closed and open flux systems, the outline of the filament and the adjacent separatrix surface brightened appreciably, possibly a signature of heating by the onset of fast breakout reconnection. Reconnection is the key mechanism that generates the jet in their model. Significantly, we observed the bidirectional flows accompanied by several brightening plasma blobs near the interaction sites. This observational evidence implies that a certain instability is in progress. In theory, several works confirmed that it is inevitable for magnetic islands to form during the magnetic reconnection process in the coronal environment of high magnetic Reynolds number (Vernazza et al. 1981; Fontenla et al. 1993; Bhattacharjee et al. 2009). On the basis of the observational findings, we consider that the plasma blobs, ejected bidirectionally along the sheet structure, are the magnetic islands/plasmoids created by the tearing mode instability as suggested by Takasao et al. (2012). Afterward, Kumar & Cho (2013) estimated the temperature and density of these plasmoids and found that the bright magnetic islands possess relatively higher temperature and density than in the surroundings. Therefore, our observed brightening blobs are extremely possibly magnetic islands occurring in the process of the external magnetic reconnection for the tearing mode instability.

This scenario is similar to the explanation that the occurrence of the tearing mode in the current sheet results in turbulence, which leads to small-scale structure that enhances the diffusion of the

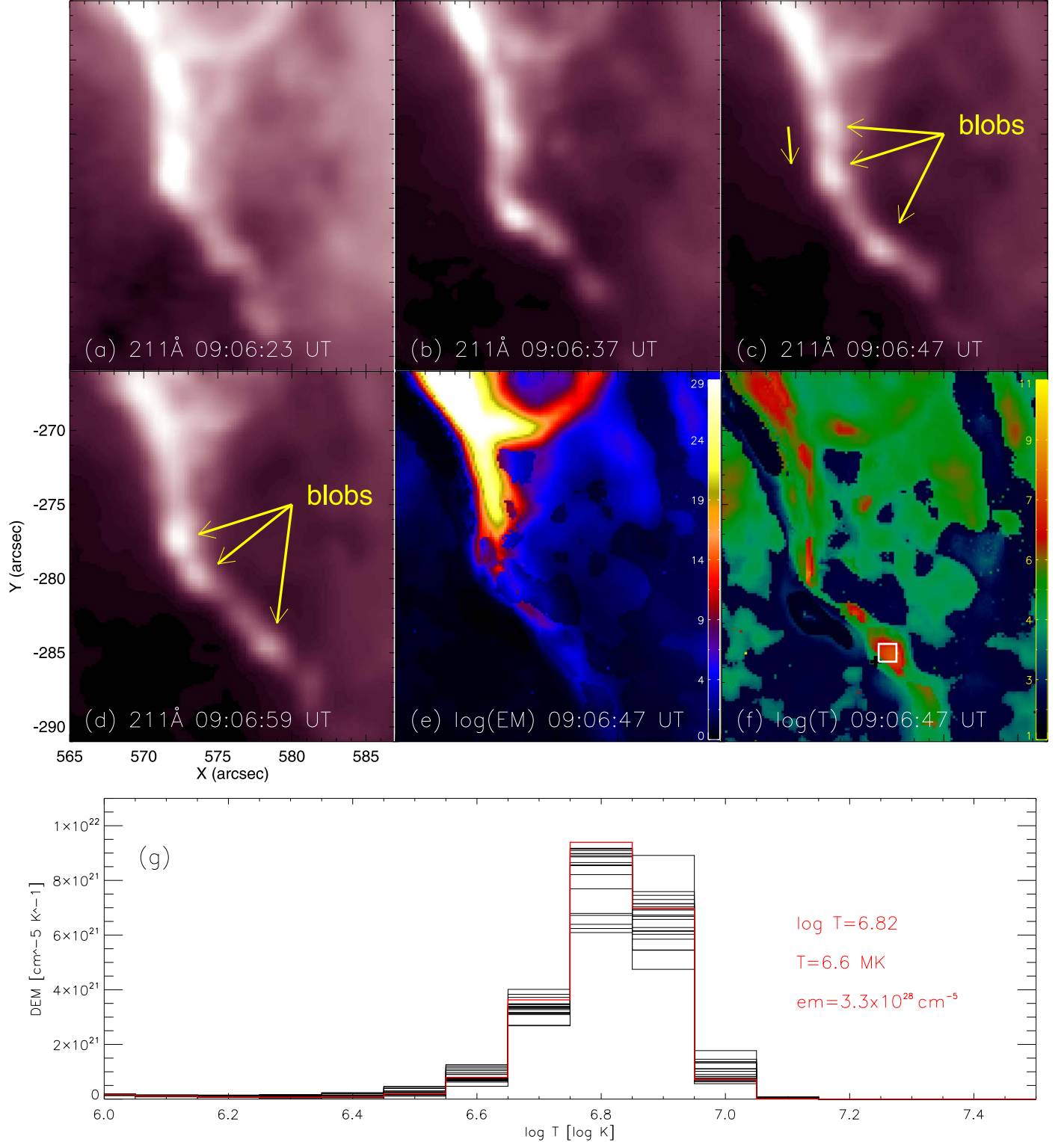


Figure 5. (a-d) AIA 211 Å images presenting the successive ejection of plasma blobs from the interacting region along the coronal loops. (e-g) DEM result of the plasma blobs near 09:06:47 UT. Panels (e)-(f) are the constructed emission measure and temperature images. Panel (g) gives the averaged DEM distribution for one of the blobs outlined by a white box with a size of 1''.2. The red curves are the best-fit DEM curves, while the black dashed distributions are 100 Monte Carlo simulations. The animated version in 211 Å images from 08:40 to 09:10 UT is compressed to a 5 s movie.

(An animation of this figure is available.)

magnetic field and thus allows the magnetic energy to be converted into heat and kinetic energy at a reasonably fast rate in a thick current sheet (Mei et al. 2012; Lin et al. 2015). This implies that there is a complex magnetic reconnection in the interaction process

to heat and transfer the material, as well as alter the magnetic topological structure of the filament. We suggested that the magnetic reconnection mediated by the tearing mode instability could indeed be triggered in the atmosphere of the Sun, which may

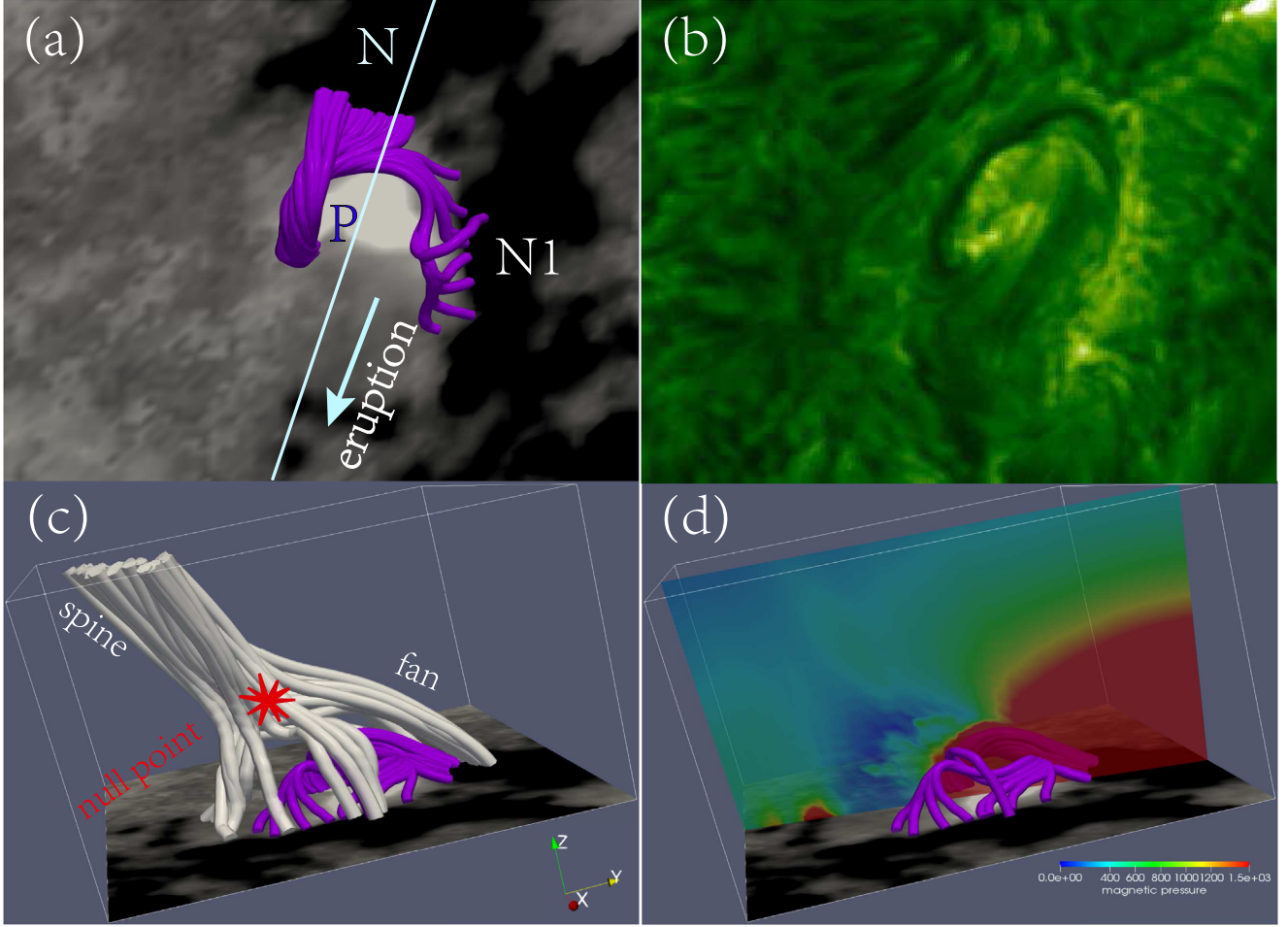


Figure 6. Magnetic topology based on NLFFF extrapolation for the eruption site. (a) The background shows the photospheric vertical magnetic field, in which a small positive polarity (P) is encircled by a negative-polarity region (N and N1). Low-lying field lines calculated from the NLFFF extrapolation at 8:48 UT are highly sheared structures that connect P with N (N1). (b) Co-temporal H α image depicting a circular filament shown for comparison. (c) The field line topology indicates the presence of a null point, complete with a dome-shaped fan and elongated spine. A red asterisk marks the locations of the null point, and the field lines are traced in its neighborhood. (d) Side view of panel (a). Magnetic pressure is imaged on a vertical cross section to illustrate its anisotropy. The cross section is roughly aligned with the direction of filament eruption (indicated by a solid line in panel (a)). A weak-field region, rendered as blue, contains the null point.

facilitate the splitting and disintegration of the filament. Similar bidirectional streaming of tearing-generated plasmoids away from the separatrix surface was detected in the high-resolution simulations of resistive-kink jets (Wyper et al. 2016).

We thank an anonymous referee for providing detailed suggestions and comments that significantly improved the presentation of this paper. We are grateful to the AIA, HMI, and NVST teams for data support. This work is supported by the Natural Science Foundation of China under grants 11703084, 11633008, 11503081, and 11703084; by the CAS programs “Light of West China” and “QYZDJ- SSW-SLH012”; and by the grant associated with the Project of the Group for Innovation of Yunnan Province.

ORCID iDs

Jiayan Yang <https://orcid.org/0000-0003-3462-4340>

References

- Asai, A., Yokoyama, T., Shimojo, M., & Shibata, K. 2004, *ApJL*, 605, L77
- Bemporad, A., Sterling, A. C., Moore, R. L., & Poletto, G. 2005, *ApJL*, 635, L189
- Bhattacharjee, A., Huang, Y.-M., Yang, H., & Rogers, B. 2009, *PhPl*, 16, 112102
- Bi, Y., Jiang, Y., Yang, J., et al. 2013, *ApJ*, 773, 162
- Bobra, M. G., Sun, X., Hoeksema, J. T., et al. 2014, *SoPh*, 289, 3549
- Borrero, J. M., Tomczyk, S., Kubo, M., et al. 2011, *SoPh*, 273, 267
- Cheng, X., Zhang, J., Saar, S. H., & Ding, M. D. 2012, *ApJ*, 761, 62
- Cirtain, J. W., Golub, L., Lundquist, L., et al. 2007, *Sci*, 318, 1580
- Fletcher, L., Metcalf, T. R., Alexander, D., Brown, D. S., & Ryder, L. A. 2001, *ApJ*, 554, 451
- Fontenla, J. M., Avrett, E. H., & Loeser, R. 1993, *ApJ*, 406, 319
- Furth, H. P., Killeen, J., & Rosenbluth, M. N. 1963, *PhFl*, 6, 459
- Haynes, A. L., & Parnell, C. E. 2007, *PhPl*, 14, 082107
- Hong, J., Jiang, Y., Yang, J., Li, H., & Xu, Z. 2017, *ApJ*, 835, 35
- Jiang, Y., Yang, J., Zheng, R., Bi, Y., & Yang, X. 2009, *ApJ*, 693, 1851
- Jiang, Y. C., Chen, H. D., Li, K. J., Shen, Y. D., & Yang, L. H. 2007, *A&A*, 469, 331
- Kliem, B., Karlický, M., & Benz, A. O. 2000, *A&A*, 360, 715
- Kumar, P., & Cho, K.-S. 2013, *A&A*, 557, A115
- Kumar, P., Karpen, J. T., Antiochos, S. K., et al. 2018, *ApJ*, 854, 155
- Leka, K. D., Barnes, G., Crouch, A. D., et al. 2009, *SoPh*, 260, 83
- Lemen, J. R., Title, A. M., Akin, D. J., et al. 2012, *SoPh*, 275, 17
- Li, H., Jiang, Y., Yang, J., et al. 2017, *ApJL*, 842, L20
- Li, H., Yang, J., Jiang, Y., et al. 2018a, *Ap&SS*, 363, 26
- Li, L., Zhang, J., Peter, H., et al. 2016, *NatPh*, 12, 847
- Li, T., Yang, S., Zhang, Q., Hou, Y., & Zhang, J. 2018b, *ApJ*, 859, 122
- Lin, J., Ko, Y.-K., Sui, L., et al. 2005, *ApJ*, 622, 1251
- Lin, J., Murphy, N. A., Shen, C., et al. 2015, *SSRv*, 194, 237
- Liu, Z., & Beckers, J. M. 2001, *Sol. Phys.*, 198, 197

- Liu, Z., Xu, J., Gu, B., et al. 2014, *RAA*, **14**, 705
 Mei, Z., Shen, C., Wu, N., et al. 2012, *MNRAS*, **425**, 2824
 Metcalf, T. R. 1994, *SoPh*, **155**, 235
 Moore, R. L., & Sterling, A. C. 2007, *ApJ*, **661**, 543
 Moreno-Insertis, F., Galsgaard, K., & Ugarte-Urra, I. 2008, *ApJL*, **673**, L211
 Ni, L., Roussev, I. I., Lin, J., & Ziegler, U. 2012, *ApJ*, **758**, 20
 Nisticò, G., Bothmer, V., Patsourakos, S., & Zimbardo, G. 2009, *SoPh*, **259**, 87
 Pariat, E., Antiochos, S. K., & DeVore, C. R. 2009, *ApJ*, **691**, 61
 Pariat, E., Antiochos, S. K., & DeVore, C. R. 2010, *ApJ*, **714**, 1762
 Pariat, E., Dalmasse, K., DeVore, C. R., Antiochos, S. K., & Karpen, J. T. 2015, *A&A*, **573**, A130
 Pesnell, W. D., Thompson, B. J., & Chamberlin, P. C. 2012, *SoPh*, **275**, 3
 Priest, E. R., & Pontin, D. I. 2009, *PhPl*, **16**, 122101
 Pontin, D. I., & Galsgaard, K. 2007, *JGRA*, **112**, A03103
 Pontin, D. I., Hornig, G., & Priest, E. R. 2004, *GApFD*, **98**, 407
 Schou, J., Scherrer, P. H., Bush, R. I., et al. 2012, *SoPh*, **275**, 229
 Shen, C., Wang, Y., Gui, B., Ye, P., & Wang, S. 2011, *SoPh*, **269**, 389
 Shen, Y., Liu, Y., Liu, Y. D., et al. 2018a, *ApJ*, **861**, 105
 Shen, Y., Liu, Y., Su, J., & Deng, Y. 2012, *ApJ*, **745**, 164
 Shen, Y., Liu, Y. D., Su, J., Qu, Z., & Tian, Z. 2017, *ApJ*, **851**, 67
 Shen, Y., Tang, Z., Li, H., & Liu, Y. 2018b, *MNRAS*, **480**, L63
 Shibata, K., Ishido, Y., Acton, L. W., et al. 1992, *PASJ*, **44**, L173
 Shimojo, M., Hashimoto, S., Shibata, K., et al. 1996, *PASJ*, **48**, 123
 Sun, X., Hoeksema, J. T., Liu, Y., Chen, Q., & Hayashi, K. 2012, *ApJ*, **757**, 149
 Takasao, S., Asai, A., Isobe, H., & Shibata, K. 2012, *ApJL*, **745**, L6
 Vernazza, J. E., Avrett, E. H., & Loeser, R. 1981, *ApJS*, **45**, 635
 Wheatland, M. S., Sturrock, P. A., & Roumeliotis, G. 2000, *ApJ*, **540**, 1150
 Wiegelmans, T. 2004, *SoPh*, **219**, 87
 Wiegelmans, T., Inhester, B., & Sakurai, T. 2006, *SoPh*, **233**, 215
 Wyper, P. F., Antiochos, S. K., & DeVore, C. R. 2017, *Natur*, **544**, 452
 Wyper, P. F., & DeVore, C. R. 2016, *ApJ*, **820**, 77
 Wyper, P. F., DeVore, C. R., & Antiochos, S. K. 2018, *ApJ*, **852**, 98
 Wyper, P. F., DeVore, C. R., Karpen, J. T., & Lynch, B. J. 2016, *ApJ*, **827**, 4
 Xu, Z., Yang, K., Guo, Y., et al. 2017, *ApJ*, **851**, 30
 Yang, L.-H., Jiang, Y.-C., Yang, J.-Y., et al. 2011, *RAA*, **11**, 1229
 Zhang, Q. M., Chen, P. F., Guo, Y., Fang, C., & Ding, M. D. 2012, *ApJ*, **746**, 19
 Zhang, Q. M., Ji, H. S., & Su, Y. N. 2016, *SoPh*, **291**, 859
 Zhang, Y. Z., & Zhang, J. 2017, *ApJ*, **834**, 79